JACS
JOURNAL OF THE AMERICAN CHEMICAL SOCIETY

Article

pubs.acs.org/JACS

Modification of Charge Trapping at Particle/Particle Interfaces by Electrochemical Hydrogen Doping of Nanocrystalline TiO_2

Juan M. Jiménez,[†] Gilles R. Bourret,[†] Thomas Berger,*[,†] and Keith P. McKenna*[,‡]

[†]Department of Chemistry and Physics of Materials, University of Salzburg, Hellbrunner Straße 34/III, A-5020 Salzburg, Austria
[‡]Department of Physics, University of York, Heslington, York YO10 5DD, United Kingdom

S Supporting Information

ABSTRACT: Particle/particle interfaces play a crucial role in the functionality and performance of nanocrystalline materials such as mesoporous metal oxide electrodes. Defects at these interfaces are known to impede charge separation via slowdown of transport and increase of charge recombination, but can be passivated via electrochemical doping (i.e., incorporation of electron/proton pairs), leading to transient but large enhancement of photoelectrode performance. Although this process is technologically very relevant, it is still poorly understood. Here we report on the electrochemical characterization and the theoretical modeling of electron traps in nanocrystalline rutile TiO_2 films. Significant changes in the electrochemical response of porous films consisting of a random network of TiO_2 particles are observed upon the electrochemical accumulation of electron/proton pairs. The reversible shift of a capacitive peak in the voltammetric profile of the electrode is assigned to an energetic modification of trap states at particle/particle interfaces. This hypothesis is supported by first-principles theoretical calculations on a TiO_2 grain boundary, providing a simple model for particle/particle interfaces. In particular, it is shown how protons readily segregate to the grain boundary (being up to 0.6 eV more stable than in the TiO_2 bulk), modifying its structure and electron-trapping properties. The presence of hydrogen at the grain boundary increases the average depth of traps while at the same time reducing their number compared to the undoped situation. This provides an explanation for the transient enhancement of the photoelectrocatalytic activity toward methanol photooxidation which is observed following electrochemical hydrogen doping of rutile TiO_2 nanoparticle electrodes.

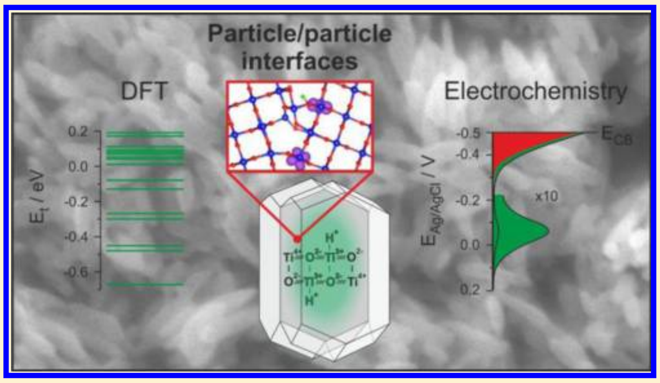

■ INTRODUCTION

Mesoporous semiconductor oxide electrodes are used in different applications including electrochemical sensing, electrochromic devices and photoelectrochemical generation of fuels or electrical energy.[1−5] All these applications rely on the external manipulation or tracking of the charge transfer between an optically and/or chemically active layer and an external contact. The macroscopic rate of charge transfer between the mesoporous film and a conductive substrate is the result of a sequence of intermingled microscopic processes. These processes, which are associated with carrier generation, recombination, transport and transfer, take place on different time scales and compete kinetically with each other. Due to a high concentration of trap states electron transport in mesoporous semiconductor oxide films is orders of magnitude slower than in single crystals. In photoelectrocatalytic and photovoltaic applications electron collection at the external contact competes with charge recombination in the bulk of the semiconductor and at the interfaces within the porous film, limiting solar conversion efficiency. The use of electrochemical doping (charge transfer reductive doping), where electron/proton or electron/Li^+ pairs incorporated within the oxide "passivate" the electron traps,[6−8] is a very efficient way to temporarily improve photoelectrochemical activity, and as such, constitutes an elegant way to improve charge separation within these materials. Although many efforts are being pursued in this direction, a comprehensive study of these electronic defects is still missing. To reach such a level of understanding, one needs to carefully identify the nature of the recombination centers and transport-limiting traps in mesoporous semiconductor electrodes, which is a significant challenge for both experimentalists and theoreticians.

It is well established that the fundamental processes associated with the transport,[9−12] transfer,[13,14] and recombination[15] of photogenerated charge carriers in mesoporous semiconductor electrodes are determined by both the distribution of band gap states and their population, i.e., the position of the Fermi level within the film. Electrochemical methods such as cyclic voltammetry and electrochemical impedance spectroscopy have proven useful in characterizing electronic states in nanostructured semiconductor oxide

Received: August 18, 2016
Published: November 13, 2016

DOI: 10.1021/jacs.6b08636
J. Am. Chem. Soc. 2016, 138, 15956−15964

electrodes, though the chemical nature of the traps remains controversial.[5,16] Specifically, charge/discharge measurements provide information on the distribution of electrochemically active states in mesoporous electrodes, where electron accumulation is compensated by the adsorption of ions at the oxide surface. For TiO_2 electrodes in an aqueous acidic electrolyte the generation of Ti^{3+} centers is compensated by proton uptake (eq 1)

$$Ti^{IV}O_2 + e^- + H^+ \leftrightarrow Ti^{III}(O)(OH) \quad (1)$$

Importantly, in the case of small cations (such as H^+ or Li^+), charge injection and compensation not only take place at the semiconductor/electrolyte interface, but can become a three-dimensional process via insertion of ions into subsurface regions of the nanocrystals. This process is often referred to as electrochemical or charge transfer reductive doping.[6,17] The reversibility of this charge accumulation opens up the possibility of driving fast reduction reactions at the semiconductor/electrolyte interface.[18] On the other hand, electrochemical doping was found to modify, at least temporarily, the electrode performance in different applications ranging from dye-sensitized solar cells[8,19,20] to photocatalysis[6−8,21−24] and supercapacitors.[25] The doping of mesoporous TiO_2 electrodes with Li (which is isovalent with H) has recently been demonstrated to enhance electron transport and improve efficiency in perovskite solar cells.[26] Whereas different studies discuss an increase of the electrode performance upon electrochemical doping phenomenologically by accelerated charge transport and reduced recombination,[6−8,19,22] the underlying microscopic details remain to be elucidated.

For TiO_2, theoretical studies have recently addressed at the single particle level the geometry and energetics of electron trap states in the bulk[27] and at the semiconductor/electrolyte interface.[28−31] Furthermore, intrinsic trapping properties of grain boundary interfaces have been studied. Deep electron traps located at the grain boundary are found to slow down charge transport unless high current densities ensure a high average occupation of transport-limiting traps.[9] Such trap filling effects have recently been highlighted for deep traps in oriented TiO_2 nanotube arrays by dynamic photocurrent measurements.[10] In addition, these states may act as recombination sites exerting a further deleterious impact on the photocurrent.[32]

The high structural and electronic complexity of mesoporous semiconductor oxide electrodes makes an investigation of the nature, concentration, and location of electronic trap states and the elucidation of their impact on charge recombination and transport very challenging. Designing appropriate model systems to understand the action of these states is difficult. Indeed, their complexity must be high enough to realistically mimic processes in technologically relevant materials, but low enough to result in clear structure−activity relationships that can be supported by both experiments and theoretical modeling.

In this work, we combine first-principles theoretical calculations with the electrochemical characterization of nanostructured rutile TiO_2 films to demonstrate that particle/particle interfaces introduce deep traps. These interfaces represent favorable locations for proton segregation, which can be induced by the electrochemical doping of the porous electrodes. A long lasting (hours to days), but reversible accumulation of electrons and protons (i.e., e^-/H^+ or H^0 doping) at the interface is tracked by cyclic voltammetry via the shift toward more positive potentials of a pair of capacitive peaks, which is associated with trap states at the particle/particle interface. The passivation of recombination centers by e^-/H^+ doping leads to a transient photocurrent enhancement due to improved electron/hole separation for those electrodes, which are characterized by a high concentration of particle/particle interfaces (i.e., random particle networks). For electrodes lacking a high density of particle/particle interfaces (i.e., arrays of oriented nanocolumns), only a minor improvement of the photocurrent is observed upon doping. This study highlights the importance of particle/particle interfaces in mesoporous films and provides strategies to actively manipulate the density of electronic states and their population by electrochemical methods. The resulting long-lasting (>15 h) improvement of photoelectrode performance after electrochemical doping is explained by using theoretical calculations that are in qualitative agreement with experiments.

■ EXPERIMENTAL SECTION

Thin Film Preparation. Slurries of rutile TiO_2 nanoparticles (Sachtleben, Nano Rutile) were prepared by grinding 1 g of TiO_2 powder with 3.2 mL of H_2O, 60 μL of acetylacetone (99+%, Aldrich), and 60 μL of Triton X (Aldrich) and were spread with a glass rod onto fluorine-doped tin oxide (FTO) conducting glass (Pilkington, TEC 15, resistance 15 $\Omega/\square$) using Scotch tape as a spacer. Alternatively, Ti foils (Goodfellow, 99.6+%, 250 μm) were used to investigate a possible impact of the substrate type on the electrochemical and photoelectrochemical properties. However, no such effect was observed for the experiments reported here. The nanoparticle (NP) films were annealed and sintered for 1 h at 450 °C in air. After sintering a film thickness of 3.5 ± 2.0 μm was determined by scanning electron microscopy (SEM). The films are formed by a random network of elongated particles with a length of ∼50 nm and a width of ∼20 nm (Figure S1a,b and ref 33) and are of pure rutile phase (Figure S2). As shown in a previous study, nanoparticles are elongated in the [001] direction. Furthermore, it was estimated that a high fraction of the exposed surface is formed by (110) facets.[33,34]

Electrodes formed by a rutile TiO_2 nanocolumn (NC) array were prepared using a hydrothermal synthesis.[35] Concretely, 21.6 mL of a 6 M HCl solution were mixed with 360 μL of Tetra-*n*-butylorthotitanat (98%, Merck Millipore). The solution was placed in a Teflon-lined steel autoclave (45 mL, Parr Instruments) containing FTO substrates and was heated to 150 °C for 15 h. After synthesis, the electrodes were thoroughly rinsed with water. These films consist of rutile TiO_2 nanocolumns with a rectangular cross section and with a width of 80−180 nm and a length of ∼1.5 μm (Figures S1c,d and S2). As highlighted previously, individual nanocolumns are porous and consist of a bundle of oriented and single crystalline nanowires with a diameter of 10−20 nm.[36] The nanowires are elongated along the [001] direction and are expected to expose (110) facets at the surface.[35] The endings of the nanowires can be observed at higher magnifications at the top parts of the nanocolumns (inset in Figure S1c).

For both types of electrode a copper wire was attached to the conducting substrates with silver epoxy. The contact area and the uncovered parts of the substrate were finally sealed by epoxy resin.

Theoretical Calculations. Spin polarized density functional theory (DFT) calculations are performed using the projector augmented wave formalism as implemented in the Vienna ab initio simulation package.[37,38] The 3d and 4s electrons of Ti, and the 2s and 2p electrons of O are treated as valence electrons and expanded in a plane wave basis with energies up to 500 eV. We use the Perdew−Burke−Ernzerhof exchange correlation functional and correct for the self-interaction error (SIE) for electrons by employing a DFT+U approach.[39] The Hubbard U parameter for the Ti 3*d*-states is taken from previous work which fitted to spectroscopic properties of surface oxygen vacancies (U_{Ti} = 4.2 eV).[40] We also employ a Hubbard U term to correct the SIE on O 2*p*-states (U_O = 7.5 eV) in order to make the results transferable to future calculations which will consider electrons

DOI: 10.1021/jacs.6b08636
J. Am. Chem. Soc. 2016, 138, 15956−15964

and holes.[41] However, we note that the addition of a Hubbard *U* term on O does not affect the calculated trapping energies reported in the present work. For the conventional cell of rutile a 6 × 6 × 9 Monkhorst–Pack k-point grid is used and structural optimization is performed until forces are less than 0.01 eV/Å. Using the Perdew–Burke–Ernzerhof exchange correlation functional we obtain lattice parameters within 2% of experiment (a = 4.67 Å and c = 3.03 Å).

To investigate the interaction of electrons with the grain boundary defect, we attempt to localize an electron polaron at all inequivalent Ti sites within the grain boundary supercell. To achieve this, we create a precursor potential well for electron trapping by displacing nearest neighbor anions away from a particular Ti site by 0.1 Å followed by full self-consistent optimization of the structure.[9,42] In cases where this displacement procedure alone is insufficient to direct the self-consistent optimization into the desired charge localized metastable state, we manually set the orbital occupancy using a modification to the VASP code developed by Allen and Watson.[43] However, we stress that in all cases the resulting metastable states are fully and self-consistently optimized. For calculations involving charged defects (such as electron polarons), overall neutrality is ensured by employing a uniform compensating charge.

To identify prospective proton incorporation sites in the grain boundary supercell, we make use of the fact that protons will form a bond with lattice oxygen ions at a distance of approximately 1.0 Å.[44] We computationally identify the set of positions within 1.0 ± 0.1 Å of each lattice oxygen ion. We further reduce the number of possible proton positions by identifying the proton positions around each oxygen ion that has the lowest electrostatic potential (thereby representing the most favorable position for the proton on electrostatic grounds). In this way, we can readily obtain a large number of prospective proton positions, which provide the initial coordinates for full geometry relaxations. Using this procedure, inequivalent proton sites with the lowest energy can be obtained systematically. This procedure is straightforward to implement and may, with suitable modification, be applicable to modeling protons in low symmetry structures (such as nanoparticles or surfaces) in a wider range of oxide materials.

■ RESULTS AND DISCUSSION

Experimental Results. Rutile TiO_2 nanoparticle (NP) electrodes (consisting of a random network of TiO_2 particles, Figure S1a,b) and nanocolumn (NC) electrodes (consisting of an array of oriented nanocolumns, Figure S1c,d) have been used in the present study as model systems for investigating the effect of nanocrystal organization and interconnection on electrochemical and photoelectrochemical properties. The voltammetric response of a rutile TiO_2 NP electrode is characterized, in the absence of significant faradaic currents (i.e., in 1 M methanol/0.1 M $HClO_4$ aqueous solution purged from O_2), by a charge accumulation region at low potentials (Figure 1a).[45] The photocurrent onset potential, which yields an estimate of the conduction band edge position in the semiconductor,[5] lies for this electrode at $E_{Ag/AgCl}$ ∼ −0.5 V (Figure S3a).

Previous analyses of the density of electrochemically active band gap states in mesoporous TiO_2 films by cyclic voltammetry and electrochemical impedance spectroscopy[5,16] have demonstrated the presence of a broad exponential distribution of states below the conduction band edge in the accumulation region in the case of anatase electrodes, which is absent in rutile TiO_2 films.[46] Currents in the accumulation region ($E_{Ag/AgCl} < -0.25$ V, Figure 1) of rutile TiO_2 electrodes have been attributed to the population/depopulation of electronic states in the conduction band compensated by proton adsorption at the oxide surface.[46] However, for both TiO_2 modifications, a narrow distribution of deep trap states is typically present and gives rise to a pair of capacitive peaks in the cyclic voltammograms (CVs), which is also observed on rutile TiO_2 NP electrodes (Figure 1a). For pristine NP electrodes, these peaks appear at $E_{Ag/AgCl}$ ∼ −0.13 V and lie thus ∼0.3–0.5 V below the conduction band edge of the semiconductor. In the following, we will focus in detail on the intensity of these signals and on the energetics of the associated trap states in mesoporous films featuring different morphology (i.e., NP versus NC films) and will follow their modification upon electrochemical doping.

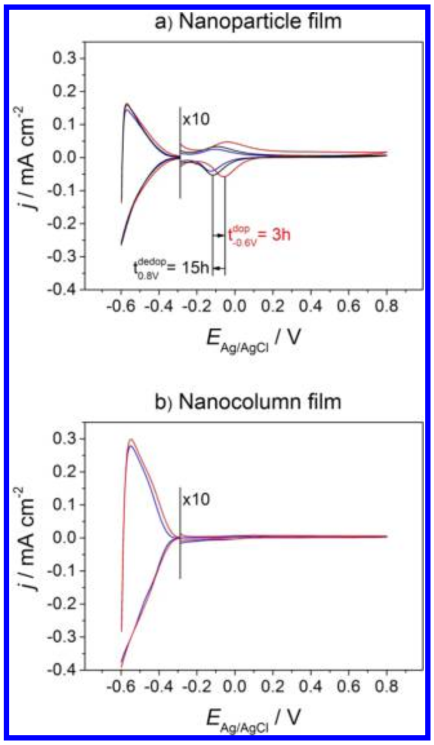

Figure 1. CVs for rutile TiO_2 NP (a) and NC (b) electrodes before and after an electrochemical doping at $E_{Ag/AgCl}$ = −0.6 V for 3 h. For the NP electrode the effect of subsequent polarization for 15 h at 0.8 V (dedoping) is also shown. Electrolyte: N_2-flushed 1 M methanol/0.1 M $HClO_4$ aqueous solution.

The intensity of the capacitive peaks depends significantly on electrode morphology. The corresponding signal is much less pronounced for the rutile TiO_2 NC electrode (Figure 1b) as compared to the NP electrode (Figure 1a). Previous studies reported that for both ordered one-dimensional nanostructures and single crystal electrodes, the peaks are virtually absent, whereas they show a high intensity for thin film electrodes consisting of random nanoparticle networks.[32,33,47] In line with previous interpretations,[32,33,47] we assign the couple of capacitive peaks observed for the NP electrode to the contribution of electron traps at particle/particle interfaces. Interestingly, the contribution is asymmetric, the anodic peak being much broader than the cathodic peak (Figures 1a and S4a). Slow kinetics for H^+ extraction (compare eq 1) or a change in the electrode conductivity may contribute to this effect. The CVs in Figure 1 were obtained by applying to the electrode a linear potential profile with a scan rate of 20 mV·s^{-1}. Importantly, at fast scan rates, it is possible that not all of the deep traps in the mesoporous film are equilibrated with the Fermi level of the conducting substrate. This is the reason why even large perturbation techniques such as cyclic voltammetry may yield for deep trap states only apparent chemical

DOI: 10.1021/jacs.6b08636
J. Am. Chem. Soc. 2016, 138, 15956−15964

capacitances.[32,48] Therefore, we performed charging and discharging measurements using extremely long lasting perturbations in the potential range featuring the capacitive peaks (Figure S5). We measured the capacitive currents upon stepping the electrode potential in potential steps $\Delta E_{Ag/AgCl}$ = 0.02 V first from 0.2 to −0.2 V (charge accumulation) and then from −0.2 V back to 0.2 V (charge extraction). After every step, the potential was kept constant for 60 s and the accumulated/extracted charge density associated with each potential step (left axis in Figure S4b) was determined by integration of the resulting current transient (Figure S5). To obtain the chemical capacitance associated with interface traps (right axis in Figure S4b) the charge was then referred to $\Delta E_{Ag/AgCl}$. Such an analysis yields a much higher symmetry of charging and discharging branches, nevertheless, there is still an imbalance of positive and negative charge pointing to a partial irreversibility of charge accumulation. The chemical capacitance extracted from these measurements (right axes in Figure S4a,b) has thus to be considered an apparent capacitance. From the total charge accumulated upon stepping the potential from 0.2 to −0.2 V (35 μC·cm^{-2}, Figure S4b), we estimate (using the average values of film thickness and particle size and assuming a film porosity of 0.5) the number of extracted charges to correspond to ∼25 electrons per TiO_2 nanoparticle.

As previously reported, TiO_2 electrodes can be electrochemically doped by cathodic polarization.[6,17] Following polarization at $E_{Ag/AgCl}$ = −0.6 V significant changes are observed in the CV of a rutile TiO_2 NP electrode (Figures 1a and S4a): the peak corresponding to deep traps is displaced by ∼0.08 V toward more positive potentials, while a slight increase of the peak intensity is observed upon doping. The same observations are made in the absence of methanol (Figure S6). Qualitatively the same conclusions can be drawn from the large perturbation charging/discharging experiment (Figure S4b). Electrochemical doping induces only minor changes at $E_{Ag/AgCl}$ < −0.2 V, although a slight increase of the capacitive current is observed at −0.45 V < $E_{Ag/AgCl}$ < −0.25 V. Importantly, we do not observe a shift of the photocurrent onset potential upon electrochemical doping (Figure S3b) indicating that the band edges are not displaced significantly. All changes in the CVs are reversible with respect to prolonged polarization at 0.8 V (t^{dedop} > 15 h, Figure 1a). These observations point to a dynamic and transient change of the density of electrochemically active states upon electrochemical charge accumulation in NP electrodes. Importantly, no significant change of the CV is observed upon doping of a NC electrode (Figure 1b).

Electrochemical doping has a beneficial effect on the photoelectrochemical performance of rutile TiO_2 NP electrodes as deduced from photocurrent transients (Figures 2a and S7) and CVs (Figure S8a). Concretely, the photocurrent generated by the electrode in a 0.1 M $HClO_4$ aqueous solution containing 1 M methanol as a hole scavenger depends significantly on the electrochemical pretreatment of the film as shown in the following. First the photocurrent of a pristine electrode was recorded at $E_{Ag/AgCl}$ = 0.8 V. Then the electrode was polarized at progressively more negative potentials in the accumulation region corresponding to the electrochemical doping of the film. After every doping step the photocurrent was again recorded to sample the impact of doping on the photoelectrocatalytic activity of the electrode. Two doping parameters were systematically changed—doping potential (Figure S7) and doping time (Figure 2). Whereas electrode polarization for 20 min at E_{dop} = −0.5 V induces only minor changes of the photoelectrocatalytic activity, we observe an up to 3-fold photocurrent increase when doping at E_{dop} = −0.6 V (Figure S7). The photocurrent enhancement by electrochemical doping is a very slow process. Only after 4 h of polarization at −0.6 V no further changes are observed in the transients (Figure 2). After such a long doping time the photocurrent has experienced an increase by a factor of ∼7 (photocurrent enhancement factor, PCEF = 7, Figure 2a).

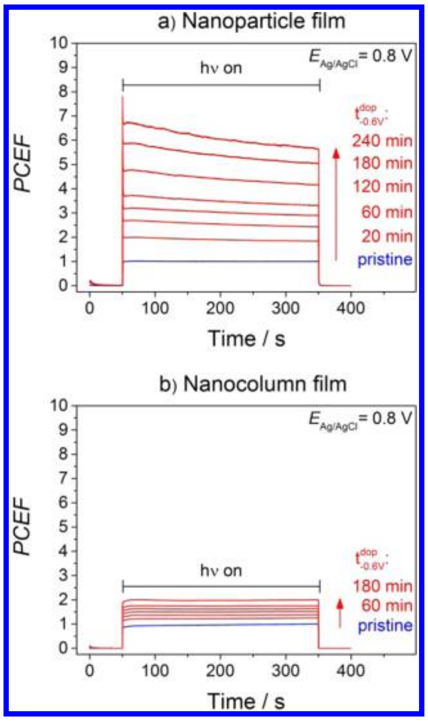

Figure 2. Photocurrent transients recorded upon UV exposure of rutile TiO_2 NP (a) and NC (b) electrodes before and after electrochemical doping at $E_{Ag/AgCl}$ = −0.6 V for different doping times ($t^{dop}_{-0.6V}$). Electrolyte: N_2-flushed 1 M methanol/0.1 M $HClO_4$ aqueous solution. Irradiance: 500 mW·cm^{-2}.

Importantly, the photocurrent increase is reversible with respect to prolonged polarization at positive potentials (Figure S8). However, even after 15 h of charge extraction (by electrode polarization at 0.8 V) the photocurrent still exceeds its initial value by ∼30%. These results highlight that the beneficial effect of electrochemical doping is transient, but long lasting.

The relative photocurrent enhancement upon doping is much less pronounced for rutile TiO_2 NC electrodes (*PCEF* = 2, Figure 2b). Also in this case the beneficial effect is reversible with respect to polarization at 0.8 V (not shown). A comparison of the photocurrent evolution following the progressive electrochemical doping of NP and NC electrodes is shown in the chronoamperometric profiles in Figure S9. Importantly, these results confirm that the increased current measured upon UV exposure of doped electrodes corresponds indeed to a faradaic photocurrent and does not simply result from a light-induced extraction of charges accumulated in the doping step. The additional charge transferred (after doping) from the TiO_2 film to the conducting substrate upon UV exposure exceeds by far the charge injected from the conducting substrate into the TiO_2 film upon electrochemical doping (Figure S9a).

From the electrochemical characterization of NP and NC films we have gained the following pieces of information about the impact of electrode morphology and electrochemical doping on the density of electrochemically active states and on the photoelectrocatalytic activity:

(i) For porous films consisting of a random particle network (NP electrodes) a high density of deep electron traps gives rise to a couple of capacitive peaks in the CV. This signal is virtually absent in films consisting of oriented nanocolumn arrays (NC electrodes).

(ii) Prolonged polarization of NP electrodes at $E_{Ag/AgCl}$ = −0.6 V (electrochemical or charge transfer reductive doping) induces a displacement of these capacitive peaks by ~0.08 V toward more positive potentials and a minor increase in the chemical capacitance at $-0.45\ V < E_{Ag/AgCl} < -0.25\ V$. These changes are reversible with respect to charge extraction (dedoping) upon prolonged electrode polarization at $E_{Ag/AgCl}$ = 0.8 V. Both processes (doping and dedoping) are extremely slow (hours to days).

(iii) Electrochemical doping increases the photoelectrocatalytic activity of NP electrodes toward methanol oxidation as sampled by a 7-fold increase of the photocurrent (PCEF = 7). The activity enhancement is transient and the photocurrent relaxes slowly back to its initial value (t^{dedop} > 15 h). The beneficial effect of electrochemical doping is much less pronounced for rutile TiO_2 NC electrodes (PCEF = 2).

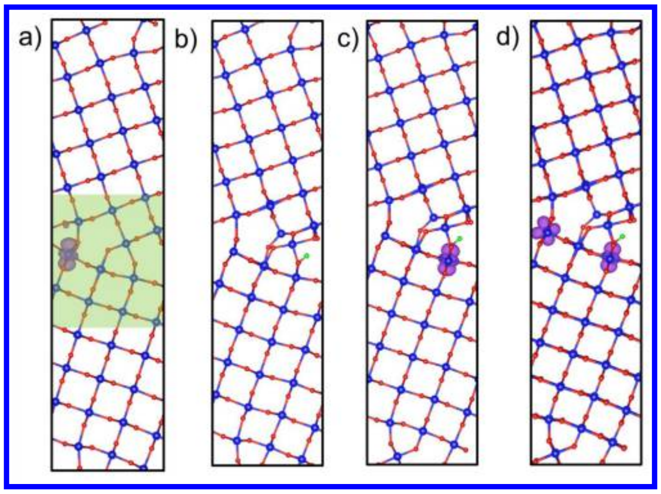

Figure 3. (a) Optimized structure of the pristine (210)[001] rutile TiO_2 grain boundary showing the electron spin density associated with an electron in the most stable site (isosurface shown in purple). The region within ±6 Å of the grain boundary is highlighted. (b) H^+ decorated (210)[001] rutile TiO_2 grain boundary. (c) $(H^+)(e^-)$ decorated (210)[001] rutile TiO_2 grain boundary. (d) $(H^+)(e^-)$ decorated (210)[001] rutile TiO_2 grain boundary with an additional electron trapped in the most stable site. Ti sites, O sites, and H^+ ions are represented by blue, red, and green spheres, respectively.

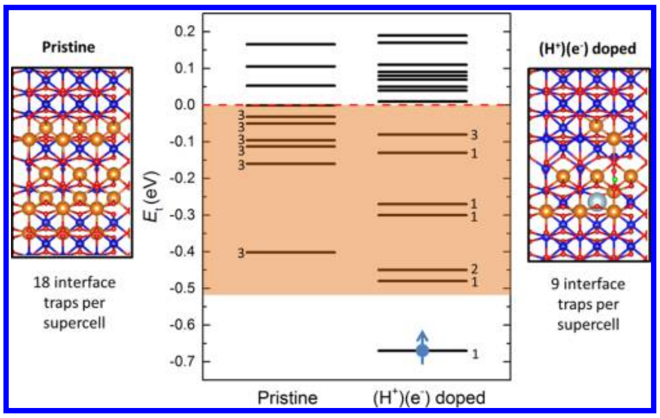

Figure 4. Distribution of electron trapping energies (E_t) within ±6 Å of the pristine and $(H^+)(e^-)$-doped grain boundary. E_t is defined with respect to the energy of an electron trapped on a bulk Ti site (horizontal dashed red line). All levels in the shaded region correspond to interfacial sites which are available to trap electrons more strongly than the bulk crystal (hereafter referred to as interface traps). The side panels show the spatial distribution of interface traps (highlighted by orange spheres). The Ti site which already has a trapped electron in the $(H^+)(e^-)$-doped interface is unavailable to trap additional electrons (indicated by the light blue sphere on the right side panel). The degeneracies of the interface traps are also shown. On $(H^+)(e^-)$-doping, the number of available interface traps is reduced by 50% (from 1.89×10^{15} to 0.95×10^{15} cm^{-2}).

Theoretical Results. To help interpret the experimental results discussed above and provide deeper atomistic insight into the effect of protons on electron trapping we perform first-principles theoretical calculations for a model interface in nanocrystalline TiO_2. In particular, we consider the (210)[001] rutile TiO_2 grain boundary, the structure of which has been investigated previously both experimentally and theoretically (Figure 3a).[49,50] While this interface possesses a high degree of symmetry it has atomistic features which are expected to be representative of more general interfaces in nanocrystalline TiO_2, namely, reduced ion coordination and local strain at the interface. In a recent theoretical study, it was demonstrated that this grain boundary is associated with interfacial Ti ions which can trap electrons more strongly than bulk Ti lattice sites.[9] This effect is due to local variations in the electrostatic potential near the grain boundary and changes in ion coordination and bond strain with similar effects found at TiO_2 surfaces.[42] Figure 4 shows the distribution of electron trapping energies (defined with respect to the energy of an electron trapped on a bulk Ti site) for Ti ions within ±6 Å of the grain boundary plane. We note that at finite temperature electrons may hop between Ti sites at the interface. The activation energy for electron hopping between adjacent sites was calculated previously to be about 0.3 eV in the bulk and up to 50% higher at the interface.[9] Owing to their increased stability the equilibrium occupation of interfacial traps will remain higher than that in the bulk. Therefore, the presence of deep traps at this interface provides a semi-quantitative model for the voltammetric feature of electron trapping states (pair of capacitive peaks) observed in the pristine TiO_2 NP electrodes by cyclic voltammetry (Figure 1a). As such it is a useful reference system on which to explore the interaction of protons with interfaces and the subsequent effect they have on electron trapping. For the following discussion, it is important to keep in mind that the energy scale and the electrochemical potential scale have opposite signs, i.e., a trap state becoming more stable (i.e., deeper) will be characterized by a more negative trapping energy and a more positive electrochemical potential.

Electrochemical doping of TiO_2 by prolonged polarization is likely to be associated with the incorporation of H^+ ions from the aqueous solution to compensate the negative electron charge trapped at interfaces. To assess this possibility we first investigate the interaction of protons with the (210)[001] rutile TiO_2 grain boundary. On introduction into the TiO_2 lattice protons form bonds with lattice O^{2-} ions resulting in OH^- species. While previous theoretical studies have identified the most stable structure of the OH^- species in bulk rutile TiO_2, it is not straightforward to deduce the likely proton configurations in the lower symmetry grain boundary region. To address this problem we identify prospective positions for H^+ incorporation based on analysis of the three-dimensional electrostatic potential and screen 80 different configurations to identify the most stable structure (see Experimental Section). For these calculations we consider one H^+ ion in a supercell of dimensions 9.1046 × 10.439 Å corresponding to a density of 1.05×10^{14} cm^{-2}. The most stable H^+ incorporation site is found at the grain boundary and is 0.6 eV more stable than in the bulk (Figure 3b). The presence of H^+ induces a transformation in structure near the grain boundary as compared to the pristine structure. In particular, one of the Ti ions near the grain boundary relaxes toward the OH^- ion.

We next investigate the interaction of electrons with the H^+ decorated grain boundary structure identified above. By making suitable initial atomic distortions around each Ti site in the supercell followed by full optimization of the total energy with respect to relaxation of all ion coordinates we obtain a series of metastable configurations corresponding to electrons trapped on different Ti ions (see Experimental Section). The most stable electron trapping Ti site is located at the grain boundary directly adjacent to the OH^- species (Figure 3c). This defect can be considered as a H^0 atom with the proton and electron dissociated onto neighboring sites. Very similar defect centers are found in nanocrystalline MgO where they have been characterized in detail by electron spin resonance and theoretical calculations.[51,52] Hereafter, we will refer to these proton plus electron defects produced by H^0 doping as $(H^+)(e^-)$ centers, following the nomenclature of previous studies. The $(H^+)(e^-)$ center should provide a reasonable model for the electron traps in the NP electrodes following electrochemical doping and polarized for sufficiently short times at a positive potential. We have also computed the Fermi contact hyperfine coupling parameter for $(H^+)(e^-)$ in the most stable position segregated at grain boundary −7.5 MHz. This is significantly reduced compared to that calculated for the isolated H atom −1402.6 MHz (close to the experimental value of 1422 MHz). This could provide an experimental signature of $(H^+)(e^-)$ centers at the grain boundary.

If each proton at the grain boundary has already trapped an electron forming a $(H^+)(e^-)$ center (as shown in Figure 3c) one may ask how additional electrons added to the system would interact with the interface (for example as realized experimentally by CV measurements on electrochemically doped electrodes). To address this question we obtain fully optimized metastable configurations corresponding to the localization of a second electron on all Ti sites in the supercell. An electron trapped on a bulk-like Ti site has a very similar local geometry and spin density to the bulk-like polaron in the pristine grain boundary. This provides a reference with which to assess the trapping energies of sites in the vicinity of the grain boundary. We find a distribution of trapping energies for Ti ions within ±6 Å of the grain boundary plane spanning a similar range to that found for the pristine interface and the most stable electron trap is again located close to the grain boundary (Figure 3d). The distribution of electron trapping energies associated with the pristine and $(H^+)(e^-)$-doped grain boundaries are compared in Figure 4. The pristine grain boundary presents 18 Ti sites per supercell that can trap electrons more strongly than in the bulk (i.e., traps with $E_t < 0$, hereafter referred to as interface traps). This corresponds to an interface trap concentration of 1.89×10^{15} cm^{-2} with an average trapping energy of −0.14 eV. Following $(H^+)(e^-)$-doping the number of interface traps is reduced dramatically. Only 9 Ti sites per supercell are found to trap electrons corresponding to an interface trap concentration of 0.95×10^{15} cm^{-2}. Analysis of atomic structures indicates that a number of effects are responsible for the modification of interfacial traps on $(H^+)(e^-)$-doping. As noted above, the presence of H^+ induces a localized deformation, which changes the structural and electrostatic environment of Ti sites near the grain boundary. We find a strong correlation between the electron trapping energy of a given Ti site and its corresponding electrostatic potential, as discussed previously for the pristine case.[9] In particular, the presence of the $(H^+)(e^-)$ center modifies the electrostatic potential on Ti sites near the grain boundary destabilizing a number of traps. At the same time one of the Ti sites adjacent to H^+ that was not a trap in the pristine case becomes a trap after doping. The net result is that the number of Ti sites available to trap electrons is reduced by 50%. The optimized atomic structures for the pristine and doped grain boundaries are provided in the Supporting Information. In addition to the reduced concentration of interface traps there is also a reduction in the average trapping energy (i.e., from −0.14 to −0.26 eV). The shift in average trapping energy of about 0.12 eV is of the same order as that observed experimentally for doped electrodes by CV (~0.08 eV, Figure 1a). Although the average depth of grain boundary traps is increased, the significant decrease in the density of interface traps provides an explanation for the improved photoelectrocatalytic activity of electrochemically doped electrodes observed experimentally.

■ GENERAL DISCUSSION

Due to the high specific surface area of mesoporous semiconductor electrodes, the main contribution to the density of electronic band gap states as sampled by electrochemical methods such as cyclic voltammetry results from processes at the semiconductor/electrolyte interface. Indeed these electrodes typically show a reversible charging/discharging behavior on short time scales. For TiO_2 electrodes the corresponding accumulated charge was shown to scale linearly with the internal area of the semiconductor/electrolyte interface.[33] Nevertheless, processes with different kinetics contribute with different relative intensities to the overall signal. Consequently, when extracting a chemical capacitance from the measured capacitive current,[16] those electronic states getting populated by very slow charging processes will be underrepresented.[48] This is true for electronic states in subsurface regions of the semiconductor, such as the electron traps at particle/particle interfaces giving rise to the pair of capacitive peaks in the CVs of rutile TiO_2 NP electrodes (Figure 1a). Importantly, whereas electrochemical methods based on charge/discharge measurements provide information on the distribution of electrochemically active states, it must not be ignored that a persistent charge accumulation in the mesoporous film may modify both the Fermi level and the density of states itself.[6,19,20] In this context, it is well established nowadays that long lasting reductive treatments of mesoporous films may result in a long lasting accumulation of charges (electrochemical or charge transfer reductive doping), thereby significantly influencing the macroscopic electrode behavior in different applications.[6−8,19−25] Whereas the technological implications of such an electrochemical manipulation of the electrode properties are

DOI: 10.1021/jacs.6b08636
J. Am. Chem. Soc. 2016, 138, 15956−15964

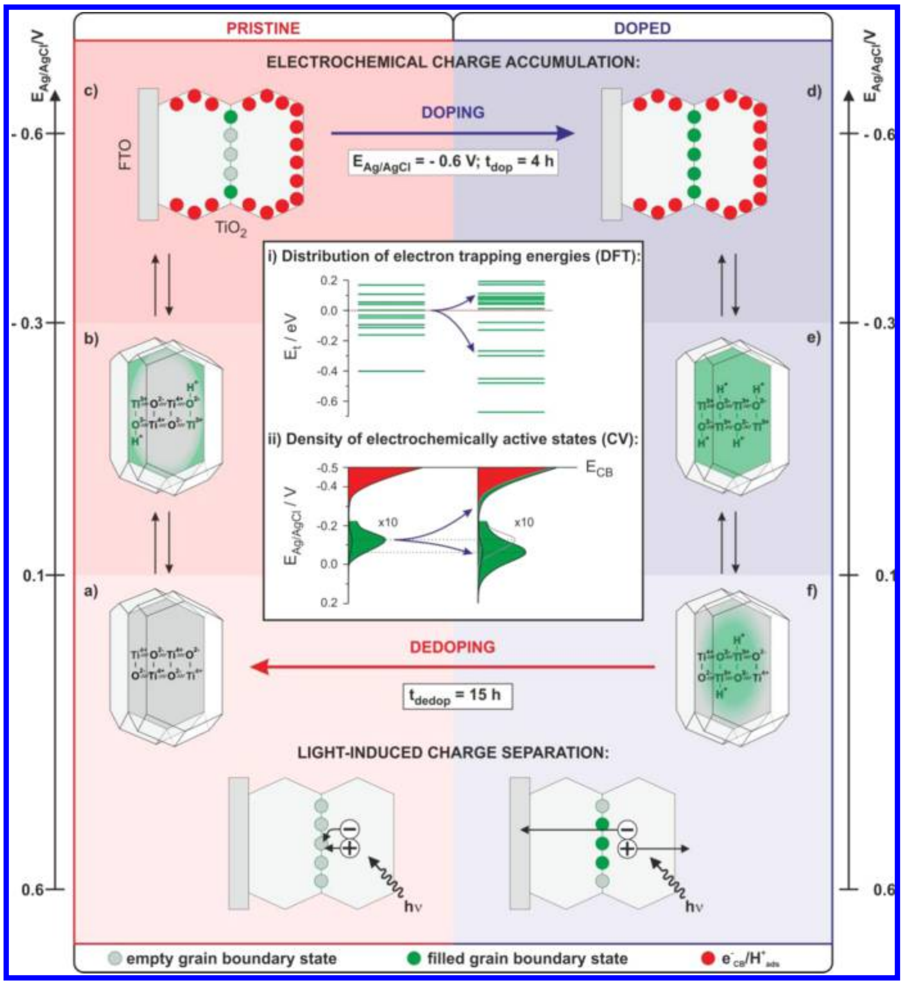

Figure 5. Scheme highlighting the effect of electrochemical doping on the density of electrochemically active states and on light induced charge separation.

clear, the underlying reasons and microscopic details of this phenomenon are unknown.

Our observations from electrochemical measurements and results from first principle theoretical calculations give a consistent picture of electron and proton trapping in nanocrystalline TiO_2 films of different morphology. The main conclusions of our study are depicted in Figure 5. Calculations indicate that $(H^+)(e^-)$ decoration modifies the distribution of electron traps at particle/particle interfaces (Figure 5i). An increase of the depth of interface traps goes along with a 50% decrease in their density. Consistent changes of the density of electrochemically active states are tracked by voltammetry (Figure 5ii). Upon electrochemical doping of rutile TiO_2 NP electrodes, i.e., upon a long lasting accumulation of electron/proton pairs in the film, we observe a reversible shift toward more positive potentials of capacitive peaks associated with trap states at particle/particle interfaces. In addition an increase of the chemical capacitance is observed at more negative potentials, i.e., at -0.45 V $< E_{Ag/AgCl} < -0.25$ V. Such a modification was previously related to the population of subsurface states upon a light-induced insertion of protons and electrons affording faster charge transport in dye-sensitized TiO_2 films.[19] Here we show that the partial removal of interface traps upon $(H^+)(e^-)$ decoration of particle/particle interfaces may contribute to such a capacitance change. The main contribution to currents in the accumulation region of both pristine and doped electrodes (contributions at $E_{Ag/AgCl} <$ -0.25 V highlighted in red in Figure 5ii), however, are associated with the population/depopulation of electronic states in the rutile TiO_2 conduction band compensated by proton adsorption at the oxide surface (e^-_{CB}/H^+_{ads} states, Figure 5c,d) as discussed in detail in a previous study.[46]

Electrochemical charge accumulation in NP electrodes is reversible on the time scale of a CV measurement, i.e. when recording the electrode's voltammetric response between 0.8 and -0.6 V (and vice versa) at a scan rate of 20 mV·s^{-1} (Figure 5a–c). In this case charge accumulation takes place mainly at the particle surface and at those grain boundary states located near the oxide/electrolyte interface. Prolonged polarization of NP electrodes at $E_{Ag/AgCl}$ = -0.6 V ($t^{dop}_{-0.6V}$ = 4 h) induces electrochemical doping and thus a population of trap states deep within the particle/particle interfaces (Figure 5 d). This charge accumulation is not reversible on the time scale of a CV measurement (Figure 5d–f). Rather there is a long lasting (though reversible, vide infra) modification of the density of electrochemically active states. In the voltammetric experiment (Figure 5d–f) charge accumulation and charge extraction take now place on a film featuring particle/particle interfaces, which are partially decorated by $(H^+)(e^-)$. Consequently, band gap states are associated with modified trapping energies resulting in a modified density of electrochemically active states (Figure 5i and ii.

The concerted uptake of e^-/H^+ pairs in particle/particle interface regions upon cathodic polarization (i.e., electron injection from the conducting substrate and insertion of protons from the electrolyte into the oxide) and the reverse process taking place upon anodic polarization (i.e., electron transfer to the substrate and proton diffusion through the solid phase into the electrolyte) are expected to proceed very slowly. Consequently, cyclic voltammetry samples only an apparent density of deep traps. The increased intensity of the pair of capacitive peaks associated with traps at the particle/particle interface can be explained by the enhanced conductivity in the doped film which allows populating and depopulating electron traps faster and deeper within the particle/particle contact area. The persistence of electrochemical doping is associated with the slow kinetics of H^+ diffusion from the GB core to the oxide/electrolyte interface. The dedoping of the film can thus only be achieved upon prolonged polarization at $E_{Ag/AgCl} > 0.2$ V (e.g., $t_{0.8V}^{dedop} = 15$ h, Figure 5a,f).

The increased photoelectrocatalytic activity of doped electrodes can be attributed to the deactivation of a major fraction of interface traps and recombination sites by the decoration of particle/particle interfaces with $(H^+)(e^-)$ (Figure 5a,f). Indeed, calculations point to a 50% decrease in density of interface traps following $(H^+)(e^-)$ doping (Figure 4), which is expected to affect charge separation at the particle/particle interface in two ways: by accelerating electron transfer across the grain boundary and by reducing electron/hole recombination. Faster electron transport in electrochemically doped TiO_2 nanoparticle films has been proven recently.[8] On the other hand, Kamat and co-workers[7] reported on the deactivation of recombination centers due to trap filling and the generation of Ti^{3+}/H^+ centers in TiO_2 electrodes. Enhancement of the transport properties of mesoporous TiO_2 electrodes for perovskite solar cells via Li doping has also been demonstrated and is proposed to involve a similar mechanism.[26] While not investigated theoretically in this work, hole trapping may also be modified in a favorable way upon $(H^+)(e^-)$ doping. Related studies are underway. Beneficial effects of electrochemical doping have been reported not only for TiO_2, but also for ZnO, WO_3, and $BiVO_4$ films.[21,24] We believe that our findings will contribute to a better understanding of interfacial processes at play in different metal oxide-based materials.

CONCLUSIONS

We have tracked the long lasting accumulation of electron/proton pairs in rutile TiO_2 films consisting of a random nanoparticle network (i) via a reversible shift of a capacitive peak in the CV, which we associate with trap states located at particle/particle interfaces, and (ii) via the transient enhancement of the photoelectrocatalytic activity toward methanol photooxidation. Theoretical calculations indicate that interfaces between crystals in TiO_2 represent favorable locations for the segregation of proton defects, being up to 0.6 eV more stable than in the bulk crystal. Importantly, $(H^+)(e^-)$ doping of grain boundaries significantly modifies the electronic properties of the particle/particle interface. For Ti ions within ±6 Å of the interface a shift in the average trapping energy of deep traps of −0.12 eV is predicted with respect to the pristine interface. A 50% reduction of the overall number of deep electron traps at the grain boundary is considered to be the main reason for the beneficial effect of electrochemical doping of rutile TiO_2 NP electrodes on their photoelectrocatalytic activity. The qualitative agreement between our experimental results and theoretical calculations strongly supports our detailed description of these complex interfacial systems.

ASSOCIATED CONTENT

Supporting Information

The Supporting Information is available free of charge on the ACS Publications website at DOI: 10.1021/jacs.6b08636.

Further experimental details, SEM images and Raman spectra of rutile TiO_2 NP and NC films, as well as further electrochemical data; electron trapping energies for interface trapping sites (PDF)

Optimized atomic structures of the pristine grain boundary (CIF)

Optimized atomic structures of the $(H^+)(e^-)$-doped grain boundary (CIF)

AUTHOR INFORMATION

Corresponding Authors

*thomas.berger@sbg.ac.at
*keith.mckenna@york.ac.uk

ORCID

Juan M. Jiménez: 0000-0001-9758-998X
Gilles R. Bourret: 0000-0002-9774-1686
Thomas Berger: 0000-0002-2062-5193

Notes

The authors declare no competing financial interest.

ACKNOWLEDGMENTS

We gratefully acknowledge support from COST Action CM1104. K.P.M. acknowledges financial support from EPSRC (EP/K003151). Via our membership of the UK's HEC Materials Chemistry Consortium, which is funded by EPSRC (EP/L000202), this work used the ARCHER UK National Supercomputing Service (http://www.archer.ac.uk). J.M.J. and T.B. acknowledge financial support from the Austrian Science Fund (FWF): [P28211−N36]. J. Winkler and B. Proft from Sachtleben Chemie GmbH (Duisburg, Germany) are acknowledged for kindly providing us with Nano-Rutile powder. Data relating to the theoretical calculations performed during this research are available by request from the University of York Research database http://dx.doi.org/10.15124/fdde4827-db8d-4491-a309-9133e7d93899.

REFERENCES

(1) Schneider, J.; Matsuoka, M.; Takeuchi, M.; Zhang, J.; Horiuchi, Y.; Anpo, M.; Bahnemann, D. W. *Chem. Rev.* **2014**, *114*, 9919−9986.
(2) Bai, Y.; Mora-Seró, I.; de Angelis, F.; Bisquert, J.; Wang, P. *Chem. Rev.* **2014**, *114*, 10095−10130.
(3) Walcarius, A. *Chem. Soc. Rev.* **2013**, *42*, 4098−4140.
(4) Bai, J.; Zhou, B. *Chem. Rev.* **2014**, *114*, 10131−10176.
(5) Berger, T.; Monllor-Satoca, D.; Jankulovska, M.; Lana-Villarreal, T.; Gómez, R. *ChemPhysChem* **2012**, *13*, 2824−2875.
(6) Berger, T.; Lana-Villarreal, T.; Monllor-Satoca, D.; Gómez, R. *Electrochem. Commun.* **2006**, *8*, 1713−1718.
(7) Meekins, B. H.; Kamat, P. V. *ACS Nano* **2009**, *3*, 3437−3446.
(8) Idígoras, J.; Berger, T.; Anta, J. A. *J. Phys. Chem. C* **2013**, *117*, 1561−1570.
(9) Wallace, S. K.; McKenna, K. P. *Adv. Mater. Interfaces* **2014**, DOI: 10.1002/admi.201400078.
(10) Zhang, Q.; Celorrio, V.; Bradley, K.; Eisner, F.; Cherns, D.; Yan, W.; Fermín, D. J. *J. Phys. Chem. C* **2014**, *118*, 18207−18213.
(11) Villanueva-Cab, J.; Jang, S.-R.; Halverson, A. F.; Zhu, K.; Frank, A. J. *Nano Lett.* **2014**, *14*, 2305−2309.

(12) Bisquert, J. *Phys. Chem. Chem. Phys.* **2008**, *10*, 49−72.
(13) Molinari, A.; Maldotti, A.; Amadelli, R. *Chem. - Eur. J.* **2014**, *20*, 7759−7765.
(14) Bisquert, J.; Zaban, A.; Greenshtein, M.; Mora-Seró, I. *J. Am. Chem. Soc.* **2004**, *126*, 13550−13559.
(15) Rex, R. E.; Knorr, F. J.; McHale, J. L. *J. Phys. Chem. C* **2014**, *118*, 16831−16841.
(16) Bisquert, J.; Fabregat-Santiago, F.; Mora-Seró, I.; Garcia-Belmonte, G.; Barea, E. M.; Palomares, E. *Inorg. Chim. Acta* **2008**, *361*, 684−698.
(17) Pelouchova, H.; Janda, P.; Weber, J.; Kavan, L. *J. Electroanal. Chem.* **2004**, *566*, 73−83.
(18) Schrauben, J. N.; Hayoun, R.; Valdez, C. N.; Braten, M.; Fridley, L.; Mayer, J. M. *Science* **2012**, *336*, 1298−1301.
(19) Wang, Q.; Zhang, Z.; Zakeeruddin, S. M.; Grätzel, M. *J. Phys. Chem. C* **2008**, *112*, 7084−7092.
(20) Fabregat-Santiago, F.; Barea, E. M.; Bisquert, J.; Mor, G. K.; Shankar, K.; Grimes, C. A. *J. Am. Chem. Soc.* **2008**, *130*, 11312−11316.
(21) Márquez, A.; Rodríguez-Pérez, M. J.; Anta, J. A.; Rodríguez-Gattorno, G.; Bourret, G. R.; Oskam, G.; Berger, T. *ChemElectroChem* **2016**, *3*, 658−667.
(22) Zhang, Z.; Hedhili, M. N.; Zhu, H.; Wang, P. *Phys. Chem. Chem. Phys.* **2013**, *15*, 15637−15644.
(23) Tsui, L.-K.; Saito, M.; Homma, T.; Zangari, G. *J. Mater. Chem. A* **2015**, *3*, 360−367.
(24) Wang, G.; Yang, Y.; Ling, Y.; Wang, H.; Lu, X.; Pu, Y.-C.; Zhang, J. Z.; Tong, Y.; Li, Y. *J. Mater. Chem. A* **2016**, *4*, 2849−2855.
(25) Li, H.; Chen, Z.; Tsang, C. K.; Li, Z.; Ran, X.; Lee, C.; Nie, B.; Zheng, L.; Hung, T.; Lu, J.; Pan, B.; Li, Y. Y. *J. Mater. Chem. A* **2014**, *2*, 229−236.
(26) Giordano, F.; Abate, A.; Correa Baena, J. P.; Saliba, M.; Matsui, T.; Im, S. H.; Zakeeruddin, S. M.; Nazeeruddin, M. K.; Hagfeldt, A.; Graetzel, M. *Nat. Commun.* **2016**, *7*, 10379.
(27) Setvin, M.; Franchini, C.; Hao, X.; Schmid, M.; Janotti, A.; Kaltak, M.; van de Walle, C. G.; Kresse, G.; Diebold, U. *Phys. Rev. Lett.* **2014**, *113*, 086402.
(28) Zhang, J.; Steigerwald, M.; Brus, L.; Friesner, R. A. *Nano Lett.* **2014**, *14*, 1785−1789.
(29) Nunzi, F.; Mosconi, E.; Storchi, L.; Ronca, E.; Selloni, A.; Grätzel, M.; De Angelis, F. *Energy Environ. Sci.* **2013**, *6*, 1221−1229.
(30) Maggio, E.; Martsinovich, N.; Troisi, A. *J. Phys.: Condens. Matter* **2016**, *28*, 074004.
(31) Selcuk, S.; Selloni, A. *Nat. Mater.* **2016**, *15*, 1107−1112.
(32) Jankulovska, M.; Berger, T.; Wong, S. S.; Gómez, R.; Lana-Villarreal, T. *ChemPhysChem* **2012**, *13*, 3008−3017.
(33) Berger, T.; Lana-Villarreal, T.; Monllor-Satoca, D.; Gómez, R. *J. Phys. Chem. C* **2007**, *111*, 9936−9942.
(34) Rotzinger, F. P.; Kesselman-Truttmann, J. M.; Hug, S. J.; Shklover, V.; Grätzel, M. *J. Phys. Chem. B* **2004**, *108*, 5004−5017.
(35) Liu, B.; Aydil, E. S. *J. Am. Chem. Soc.* **2009**, *131*, 3985−3990.
(36) Wang, G.; Wang, H.; Ling, Y.; Tang, Y.; Yang, X.; Fitzmorris, R. C.; Wang, C.; Zhang, J. Z.; Li, Y. *Nano Lett.* **2011**, *11*, 3026−3033.
(37) Kresse, G.; Furthmüller, J. *Phys. Rev. B: Condens. Matter Mater. Phys.* **1996**, *54*, 11169−11186.
(38) Kresse, G.; Furthmüller, J. *Comput. Mater. Sci.* **1996**, *6*, 15−50.
(39) Dudarev, S. L.; Botton, G. A.; Savrasov, S. Y.; Humphreys, C. J.; Sutton, A. P. *Phys. Rev. B: Condens. Matter Mater. Phys.* **1998**, *57*, 1505−1509.
(40) Morgan, B. J.; Watson, G. W. *Surf. Sci.* **2007**, *601*, 5034−5041.
(41) McKenna, K. P.; Wolf, M. J.; Shluger, A. L.; Lany, S.; Zunger, A. *Phys. Rev. Lett.* **2012**, *108*, 116403.
(42) Wallace, S. K.; McKenna, K. P. *J. Phys. Chem. C* **2015**, *119*, 1913−1920.
(43) Allen, J. P.; Watson, G. W. *Phys. Chem. Chem. Phys.* **2014**, *16*, 21016−21031.
(44) Bjørheim, T. S.; Stølen, S.; Norby, T. *Phys. Chem. Chem. Phys.* **2010**, *12*, 6817−6825.
(45) Fabregat-Santiago, F.; Mora-Seró, I.; Garcia-Belmonte, G.; Bisquert, J. *J. Phys. Chem. B* **2003**, *107*, 758−768.
(46) Jankulovska, M.; Berger, T.; Lana-Villarreal, T.; Gómez, R. *Electrochim. Acta* **2012**, *62*, 172−180.
(47) Lana-Villarreal, T.; Mao, Y.; Wong, S. S.; Gómez, R. *Nanoscale* **2010**, *2*, 1690−1698.
(48) Bertoluzzi, L.; Herraiz-Cardona, I.; Gottesman, R.; Zaban, A.; Bisquert, J. *J. Phys. Chem. Lett.* **2014**, *5*, 689−694.
(49) Wallis, D. J.; Browning, N. D.; Nellist, P. D.; Pennycook, S. J.; Majid, I.; Liu, Y.; Vander Sande, J. B. *J. Am. Ceram. Soc.* **1997**, *80*, 499−502.
(50) Dawson, I.; Bristowe, P. D.; Lee, M.-H.; Payne, M. C.; Segall, M. D.; White, J. A. *Phys. Rev. B: Condens. Matter Mater. Phys.* **1996**, *54*, 13727−13733.
(51) Ricci, D.; Di Valentin, C.; Pacchioni, G.; Sushko, P. V.; Shluger, A. L.; Giamello, E. *J. Am. Chem. Soc.* **2003**, *125*, 738−747.
(52) Chiesa, M.; Paganini, M. C.; Giamello, E.; Murphy, D. M.; Di Valentin, C.; Pacchioni, G. *Acc. Chem. Res.* **2006**, *39*, 861−867.